# The effect of graphene and graphene oxide induced reactive oxygen species on polycaprolactone scaffolds for bone cancer applications

Yanhao Hou [a], Weiguang Wang [a],[**], Paulo Bartolo [a],[b],[*]

[a] School of Engineering, Faculty of Science and Engineering, The University of Manchester, Manchester, UK
[b] Singapore Centre for 3D Printing, School of Mechanical and Aerospace Engineering, Nanyang Technological University, Singapore, Singapore

## ARTICLE INFO

## ABSTRACT

Bone cancer remains a critical healthcare problem. Among current clinical treatments, tumour resection is the most common strategy. It is usually effective but may present several limitations such as multiple operations, long hospital time, and the potential recurrence caused by the incomplete removal of cancer cells. To address these limitations, three-dimensional (3D) scaffolds fabricated through additive manufacturing have been researched for both bone cancer treatment and post-treatment rehabilitation. Polycaprolactone (PCL)-based scaffolds play an important role in bone regeneration, serving as a physical substrate to fill the defect site, recruiting cells, and promoting cell proliferation and differentiation, ultimately leading to the regeneration of the bone tissue without multiple surgical applications. Multiple advanced materials have been incorporated during the fabrication process to improve certain functions and/or modulate biological performances. Graphene-based nanomaterials, particularly graphene (G) and graphene oxide (GO), have been investigated both *in vitro* and *in vivo*, significantly improving the scaffold's physical, chemical, and biological properties, which strongly depend on the material type and concentration. A unique targeted inhibition effect on cancer cells was also discovered. However, limited research has been conducted on utilising graphene-based nanomaterials for both bone regeneration and bone cancer treatment, and there is no systematic study into the material- and dose-dependent effects, as well as the working mechanism on 3D scaffolds to realise these functions. This paper addresses these limitations by designing and fabricating PCL-based scaffolds containing different concentrations of G and GO and assessing their biological behaviour correlating it to the reactive oxygen species (ROS) release level. Results suggest that the ROS release from the scaffolds is a dominant mechanism that affects the biological behaviour of the scaffolds. ROS release also contributes to the inhibition effect on bone cancer due to healthy cells and cancer cells responding differently to ROS, and the osteogenesis results also present a certain correlation with ROS. These observations revealed a new route for realising bone cancer treatment and subsequent new bone regeneration, using a single dual-functional 3D scaffold.

## 1. Introduction

Tumour resection remains the primary clinical treatment approach for bone cancer, followed by chemotherapy and radiotherapy or a combination of them [1]. However, despite the clinical intervention, the fatality and recurrence rate is still high as cancer cells are difficult to be completely removed even though the tumour resection area tends to be larger than the diagnosed tumour size [2,3]. Moreover, current strategies present significant side effects, including hair loss, diarrhea, anaemia, infections, high cost, and relatively long treatment periods [4].

The bone regeneration outcome also varies with gender and decreases with age [5,6].

Recent advances in scaffold-based bone tissue engineering and advanced materials allow the development of novel approaches for cancer recurrence prevention and bone tissue regeneration, including the direct use of functional materials carried by 3D printed bone scaffolds and the fabrication of 3D printed scaffolds that serve as the medium for photothermal/magnetothermal therapy [4].

Nanomaterials such as graphene-based nanomaterials have been extensively explored for biomedical purposes. Because of the scale, these

* Corresponding author. School of Engineering, Faculty of Science and Engineering, The University of Manchester, Manchester, UK.
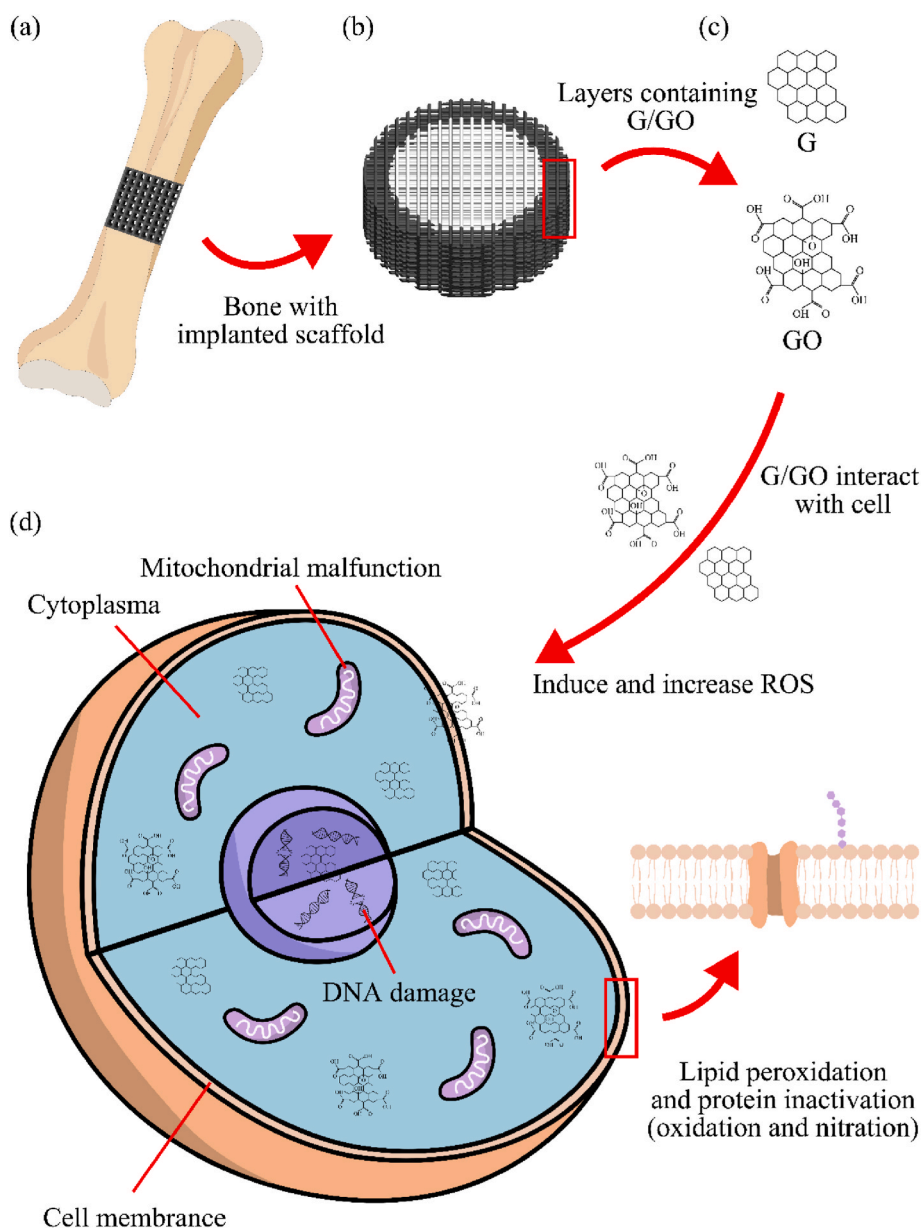** Corresponding author.
*E-mail addresses:* weiguang.wang@manchester.ac.uk (W. Wang), pbartolo@ntu.edu.sg, paulojorge.dasilvabartolo@manchester.ac.uk (P. Bartolo).

**Scheme 1.** (a) Bone with tumour removed after surgery, implanted with the dual-functional scaffold. (b) Dual-functional scaffold with external layers (polymer matrix mixed with anticancer fillers) and internal layers (biocompatible and bioactivity polymeric material). (c) Potential residual and recurrent cancer cells contact and react with the G/GO external layers leading to the formation and increase of ROS. (d) The increased ROS leads to mitochondrial malfunction (permeabilization and release of cytochrome *c*), lipid peroxidation, intracellular protein inactivation (oxidation and nitration), affecting nucleic acids, and eventually apoptosis or necrosis.

nanomaterials can easily penetrate the cell membrane, endocytosed by cells, and react with cells, or deliver certain drugs to cells. Among these nanomaterials, graphene-based nanomaterials, such as pristine graphene (G), graphene oxide (GO), and reduced graphene oxide (rGO), showed unique advantages [7,8]. G has a high-aspect ratio with the single-dimensional or few two-dimensional layered carbon atoms organised in a hexagonal lattice [9,10]. Carbon atoms are sp$^2$ (planar) hybridized, having covalent σ bonds with the three closest carbon atoms, presenting Young's modulus of ~1 TPa [11,12]. G can be synthesised through top-down methods by detaching or exfoliating from existing graphite crystals, such as by mechanical exfoliation (repeated peeling) and liquid-phase exfoliation [13,14]. Bottom-up synthesis methods, such as epitaxial growth on silicon carbide crystals and chemical vapour deposition, produce G by growing G layers on substrate surfaces [15,16]. Main G derivatives include GO and rGO. GO can be

obtained through the oxidation of G, and rGO can be further obtained by the reduction of GO with chemicals [17]. GO has up to 50 % oxygen content while rGO results in significantly lower oxygen content although a complete reduction has not yet been achieved [9,11,18].

These graphene-based materials have been successfully used for biomedical applications, presenting significant modulation effects on the biological behaviour of cells. The high specific surface area and the presence of functional groups (e.g. oxygen, hydroxyl, and carboxyl) make graphene-based nanomaterials characterised by high biomolecule adsorption [10]. The protein adsorption affects the reactions of these nanomaterials in the biological environment [19,20], including attachment, proliferation, and even differentiation [21].

The cytotoxic mechanism of graphene-based nanomaterials comprises both the direct contact between the material and cell, and the indirect reactive oxygen species (ROS) and consequent oxidative stress
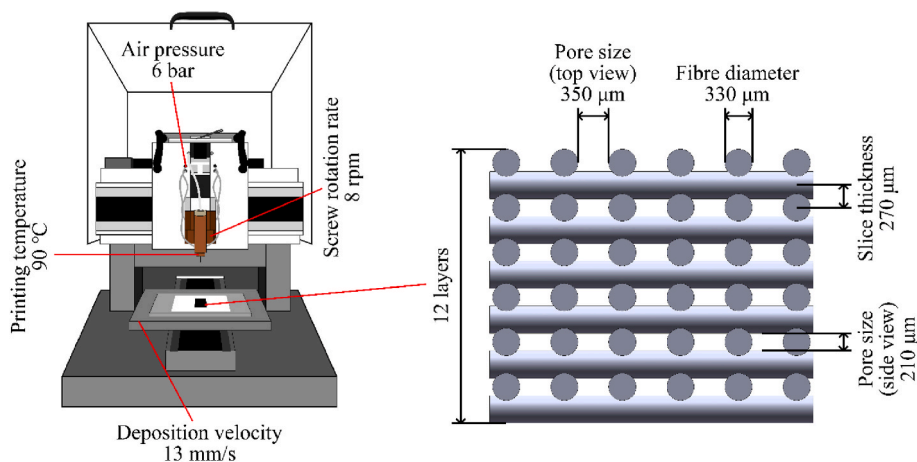
**Fig. 1.** Schematic representation of both fabrication system and scaffold. Considered processing parameters (nozzle diameter of 330 μm, printing temperature of 90 °C, air pressure of 6 bars, deposition velocity of 13 mm/s, and screw rotational velocity of 8 rpm, and layer thickness of 270 μm) and scaffold design parameters (0°/90° lay-down pattern, 330 μm fibre diameter, 350 μm top view pore size, and 210 μm side view pore size).

induced by the graphene-based nanomaterials [22]. Due to the direct contact between graphene-based nanomaterials and live cells, these nanomaterials can cut and go through cell membranes, leading to direct membrane damage [23]. These interactions increase with the degree of oxidization and the size of graphene-based nanomaterials [24]. Because of the strong adsorptions between graphene-based nanomaterials and lipid molecules, the contact between the material and cell membrane extracts phospholipids from the lipid bilayer [25,26]. Graphene-based nanomaterials can also interfere with or damage DNA or RNA by preferentially adsorbing single-stranded over double-stranded forms, protecting adsorbed nucleotides from nuclease enzymes attack, and affecting cellular signalling transmission and network functionality [27, 28].

Moreover, graphene-based nanomaterials, particularly those adsorbed on the cell surface and passed through the membrane into the cell, can induce ROS and consequent oxidative stress, which were reported to be the dominant mechanism causing cell toxicity (Scheme 1) [29]. Adenosine triphosphate is produced by reducing molecular oxygen to water via a series of coupled proton and electron transfer reactions in cell mitochondria. The residual oxygen, which is not completely reduced, forms superoxide anion radicals, and subsequently other ROS (mainly oxygen-containing radicals) [30]. These metabolic by-products (ROS) include superoxide radicals, hydrogen peroxide, hydroxyl radicals, and singlet oxygen [31,32]. The reducing equivalents, including enzymatic components such as superoxide dismutase, catalase, and glutathione peroxidase, can prevent cells from ROS-induced cellular damage by breaking down and removing ROS (free radicals) [33]. The balance of ROS and reducing equivalents is important and the intracellular ROS level needs to be kept at a critical level due to many processes, such as protein phosphorylation, transcription factor activation, apoptosis, immunity, and differentiation, which depend on sufficient level of ROS production and intracellular presence [34,35]. When the ability of cells to eliminate free radicals cannot match the formation of free radicals, the ROS accumulate intracellularly and raise oxidative stress [36,37]. ROS and oxidative stress lead to mitochondrial malfunction (permeabilization and release of cytochrome *c*), lipid peroxidation, intracellular protein inactivation (oxidation and nitration), affecting nucleic acids, and eventually apoptosis or necrosis [37,38]. Researchers utilised ROS to promote cancer treatment for Hela cells, lung cancer cells, brain glioma cells, and mammary gland cancer cells [39]. However, only limited research has been conducted on bone cancer treatment, and the correlation among the material type, dose, and biological effects on bone tissue engineering scaffolds is still not clear.

A novel concept of dual-functional scaffolds, containing external layers that are responsible for the inhibition of the residual cancer cells and preventing recurrence, and internal layers that are responsible for bone tissue regeneration, was proposed previously by our group (Scheme 1) [40,41]. Authors demonstrated the feasibility of using graphene-based nanomaterials, G and GO, as functional fillers to improve the mechanical, surface, and modulate biological properties [40,41]. However, these results were limited to relatively low concentrations of G/GO, and high concentrations of G, respectively. Therefore, it was not possible to understand the effect of each functional filler across a large spectrum of concentrations. Additionally, those papers did not investigate the mechanisms responsible for the decrease in cell viability for large concentrations of functional fillers, although the potential mechanism (effect of ROS) has been proposed.

To address these limitations, this paper aims to provide a deeper understanding of the biological effects of functional filler and its corresponding mechanism of how G and GO induced ROS affect cell metabolic activity and osteogenesis differentiation, comparing G and GO over a wider range of concentrations (from the lowest 1 wt% to the highest 7 wt%), which was not done in the past studies. Thus, a comprehensive study was conducted. Different concentrations of G and GO were incorporated into PCL to fabricate bone tissue engineering scaffolds through additive manufacturing with accurate control over the material dose and structure topology. Besides, both human adipose-derived stem cells (hADSCs) and sarcoma osteogenic (Saos-2) cells are considered for the investigation of *in vitro* recurrence prevention stages, evaluating the correlation between cell viability and ROS release level, and the targeting effects, according to different material type and dose. Moreover, hADSCs were also considered for the assessment of *in vitro* bone regeneration stages to evaluate the osteogenic differentiation ability of the scaffolds and the correlation with ROS release level, according to different material types and doses. Finally, the critical concentration thresholds are identified for inhibiting cancer cells and promoting bone tissue regeneration, revealing the dose-dependent effect and material-dependent effect can be correlated to the G and GO induced ROS.

## 2. Methods

### 2.1. Scaffold design and fabrication

PCL pellets (Capa 6500, Perstorp, UK), G nanosheets (Sigma-Aldrich, UK), and GO nanosheets (Sigma-Aldrich, UK) were used as received from suppliers. The melt-blending method was used to prepare PCL/G

and PCL/GO composite materials at desired concentrations (1, 3, 5, and 7 wt%, corresponding to G1, G3, G5, G7, GO1, GO3, GO5, and GO7 respectively). Briefly, PCL pellets and corresponding graphene-based nanomaterials (G and GO) were weighted at desired concentrations and heated to 150 °C in a crucible. The mixture was stirred for 30 min to guarantee evenly dispersion. After 2 h of cooling, the mixed materials were cut into small pieces for printing. As shown in Fig. 1, scaffolds with a 0°/90° lay-down pattern architecture, 330 μm fibre diameter, and 350 μm top view and 210 μm side view pore size, were fabricated using 3D Discovery (regenHU, Switzerland), a screw-assisted material-extrusion additive manufacturing system, at room temperature and with the optimal processing parameters previously reported (nozzle diameter of 330 μm, printing temperature of 90 °C, air pressure of 6 bars, deposition velocity of 13 mm/s, and screw rotational velocity of 8 rpm, and layer thickness of 270 μm) [40–42]. The geometrical characteristics of the considered scaffolds were based on previous studies from our group that investigated the effect of filament diameter, pore size, and porosity on mechanical and biological properties [42–45]. As reported the considered values are the ones that allow both high mechanical properties and cell attachment, proliferation, and differentiation.

All fabricated scaffolds were then morphologically analysed through scanning electron microscopy (SEM) to compare the obtained geometrical characteristics (e.g. fibre diameter, pore size, and porosity) with the designed values. The produced scaffolds had the fibre diameter of 335.0 $\pm$ 17.9 μm, pore size of 350.0 $\pm$ 12.3 μm (top view) and 216.3 $\pm$ 32.4 μm (side view), and porosity of 48.8 %, close to the designed values (Supplementary Material Fig. S1 and Table S1).

### 2.2. Cell culture and cell seeding

hADSCs (Invitrogen, USA) (passage 4–6) and Saos-2 cells (ATCC, USA) (passage 4–6) were considered for *in vitro* biological studies. During the culture, seeding, metabolic activity, and ROS release study, MesenPRO RS Basal medium (Thermo Fisher Scientific, USA) was used for hADSCs and McCoy's 5A Medium (Thermo Fisher Scientific, USA) was used for Saos-2 cells. During osteogenic differentiation and ROS release evaluation, StemPro Osteogenesis Differentiation Kit (Thermo Fisher Scientific, USA) was used for hADSCs. The medium was changed every two days for both cell types in all processes. Before cell seeding, cells were thawed from liquid nitrogen, cultured with the corresponding medium, and harvested at approximate 80 % confluence. The scaffolds were trimmed, sterilized (first 70 % ethanol then Dulbecco's Phosphate-Buffered Saline (PBS) (Thermo Fisher Scientific, USA)), air-dried, and seeded with ~20000 cells (in 400 μl of medium) on each scaffold. The cell-seeded scaffolds were then cultured under standard conditions (37 °C, 5 % CO2 concentration, and 95 % humidity) according to the suppliers' instructions.

### 2.3. Cell metabolic activity evaluation

Both hADSCs and Saos-2 cells were considered for cell metabolic activity. The cell metabolic activity was measured through Alamar Blue assay using resazurin sodium salt (Sigma-Aldrich, UK) after 1, 3, 7, and 14 days of cell seeding. The fluorescence intensity of the assay is proportional to the amount of metabolically active cells. Each cell-seeded scaffold was added with 400 μl medium containing 0.001 % resazurin sodium salt on each day. After 4 h of incubation under standard conditions, 150 μL medium was collected from each well and the fluorescence intensity was measured by a CLARIOstar microplate reader (BMG LABTECH, Germany) at 540 nm excitation and 590 nm emission wavelength.

### 2.4. Osteogenic differentiation evaluation

hADSCs were considered for osteogenic differentiations. After 7 days of proliferation in the basal medium, cells were differentiated in the osteogenesis differentiation medium for further 7 days (corresponding to day 14 in differentiation results) and 14 days (corresponding to day 21 in differentiation results).

The alkaline phosphatase (ALP) enzymatic activity was measured by the SensoLYTE® pNPP Alkaline Phosphatase assay kit (AnaSpec, USA). At each time point, scaffolds were washed (first PBS then assay buffer), transported to 15 ml centrifuge tubes, and added with 0.8 mL assay buffer containing 0.2 % (v/v%) Triton X-100. Each scaffold was vortexed for 1 min, sonicated for 2 min, stored under −80 °C for 15 min, and thawed at room temperature. Then all scaffolds were centrifuged under 2500 g for 10 min at 4 °C. To measure the activity of protein phosphatases, 50 μl supernatants were collected from each well and added with 50 μl p-nitrophenyl phosphate. After incubation for 1 h at room temperature, a stop solution was added to each well and the absorbance was measured at 405 nm by a CLARIOstar microplate reader. The total protein concentration was measured by the Micro BCA Protein assay kit (Thermo Fisher Scientific, USA). Briefly, after centrifugation, 75 μl supernatants were collected from each well and added with 75 μl working solution. After incubation for 2 h in dark at 37 °C, the plate was cooled to room temperature and the absorbance was measured at 562 nm by a CLARIOstar microplate reader. The ALP enzymatic activity was evaluated using a standard curve and normalized to the total protein.

The calcium deposition process was determined using Alizarin Red-S (ARS, Sigma-Aldrich, UK) staining. At each time point, scaffolds were washed and immersed in 10 % neutral formaldehyde solution (Sigma-Aldrich, UK) for 15 min. The scaffolds were rinsed with deionized water, added with 0.2 % ARS staining dye, and incubated at room temperature for 40 min. Then scaffolds were rinsed with deionized water, transferred into 15 mL centrifuge tubes, and added with 0.8 mL 10 % acetic acid. After standing for 30 min with gentle vibration, the scaffolds were heated to 85 °C for 10 min and placed on ice for 5 min. After centrifuging under 2500 g for 15 min, 400 μL supernatants were collected, added with 150 μL of 10 % ammonium hydroxide, adjusting the pH value to 4.1–4.5, and measured at an absorbance of 405 nm by a CLARIOstar microplate reader.

### 2.5. ROS release evaluation

The ROS release was evaluated considering both hADSCs and Saos-2 cells using the DCFDA cellular ROS assay kit (Abcam, UK) after 3, 7, and 14 days of cell seeding during the proliferation period, and after 14 and 21 days of cell seeding during the differentiation period. The medium was removed at each time point, and the scaffolds were rinsed with PBS and added with 300 μl DCFDA solution at 10 μM. After 45 min of incubation in dark at 37 °C, the DCFDA solution was removed and added with DCFDA assay buffer. The fluorescence intensity was measured using a CLARIOstar microplate reader at 485 nm excitation and 535 nm emission wavelength. The cell-seeded scaffolds were also imaged using a Leica SP8 LIGHTNING confocal microscope (Leica, Germany).

### 2.6. Cell morphology evaluation

Cell morphology was investigated using confocal microscope imaging. Cell-seeded scaffolds were fixed in 10 % neutral formaldehyde solution for 30 min, rinsed with PBS, and added with 0.1 % Triton X-100 (Sigma-Aldrich, UK) for 5 min at room temperature. Then 8 % w/w fetal bovine serum (Sigma-Aldrich, UK) in PBS was added for 1 h. The scaffolds were first stained with Alexa Fluor 594 phalloidin (Thermo Fisher Scientific, USA) in 1 % FBS solution in dark at room temperature for 40 min and then stained with 4′,6-diamidino-2-phenylindole (DAPI, Thermo Fisher Scientific, USA) in dark at room temperature for 5 min, according to the suppliers' instructions. A Leica SP8 LIGHTNING confocal microscope was used for imaging.

Cell morphology and calcium deposition were also investigated using scanning electron microscopy (SEM) imaging. Cell-seeded scaffolds were fixed in 10 % neutral formaldehyde solution for 30 min and
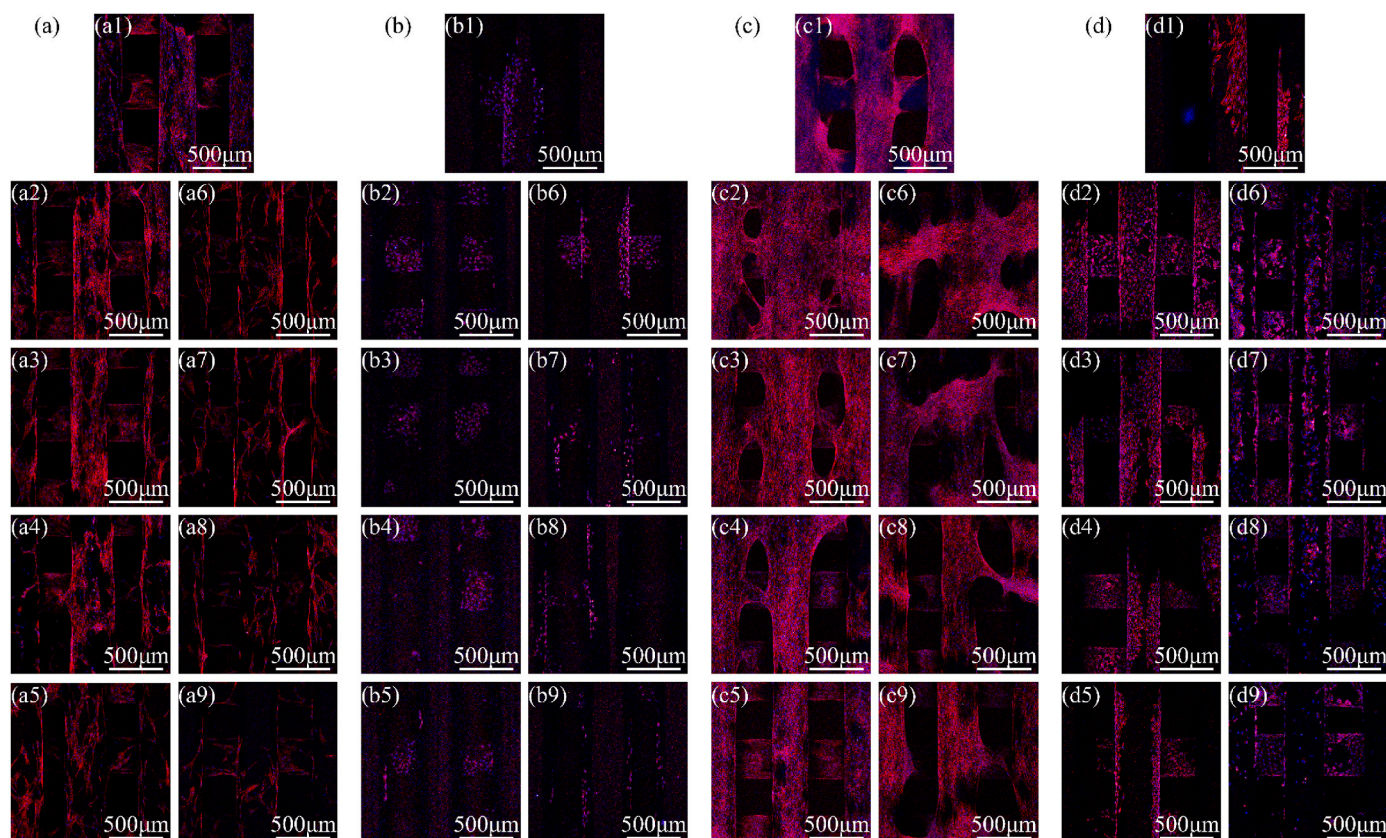
**Fig. 2.** Confocal images of hADSCs (a and c) and Saos-2 (b and d) cells on PCL, G, and GO scaffolds after 7 (a and b) and 14 (c and d) days of cell seeding. (1) PCL, (2–5) G1, G3, G5, and G7, (6–9) GO1, GO3, GO5, and GO7. Nuclei is stained blue and cell actin is stained red.

dehydrated in ethanol with graded concentrations (50 %, 60 %, 70 %, 80 %, 90 %, and 100 % twice) for 15 min for each concentration. Then the scaffolds were dehydrated using hexamethyldisilazane (HMDS, Sigma-Aldrich, UK) and ethanol (1:1) mixture for 15 min, followed by 100 % HMDS and dry overnight. The scaffolds were coated with 5 nm of gold-palladium (80:20) using a Q150T ES sputter coater (Quorum Technologies, UK). A TESCAN MIRA3 system (TESCAN, Czech Republic) was used to image the top surface, cross-section, and close-up view at a 2 kV accelerating voltage. The EDX results were also obtained using the same system at a 15 kV accelerating voltage.

### 2.7. Statistical analysis

All experiments were conducted with at least three scientific repeats ($n \geq 3$) and the results are reported as mean ± standard deviation. All results were statistically analysed through one-way ANOVA with Tukey post-hoc tests using the Origin software (OriginLab, USA) and the significance levels were set at * $P < 0.05$, **$P < 0.01$, and ***$P < 0.001$ comparing with PCL, #$P < 0.05$, ##$P < 0.01$, and ###$P < 0.001$ comparing among the same material with different concentrations, & P $< 0.05$, && $P < 0.01$, and &&& $P < 0.001$ comparing between different materials with the same concentration.

### 3. Results

#### 3.1. Cell metabolic activity evaluation and ROS release during proliferation

Confocal microscope images (Fig. 2) and SEM images (Supplementary Material Figs. S2 and S3) present the cell morphology on the scaffolds, showing that both hADSCs and Saos-2 cells were able to be sustained by the scaffolds and proliferate on the scaffold, both along the

fibres and bridging between fibres. As shown in Fig. 3, the metabolic activity measured on day 1 after cell seeding suggested that cells have been successfully seeded on the scaffolds, and the metabolic activity of both cells on PCL scaffolds was regarded as the normalisation reference to compensate for the potential differences during cell seeding and the response to the assay. Moreover, in comparison to day 1, a significantly higher metabolic activity of both types of cells was observed on all scaffolds on day 14, demonstrating significant cell growth and proliferation. However, the increasing trend varies with materials and concentrations. In the case of both hADSC and Saos-2 cells, the highest cell viability was observed on G1 and the lowest on GO7 scaffolds on day 14, indicating that the cell metabolic activity is material type- and concentration-dependent.

Cell metabolic activity was analysed and correlated with the ROS release to assess the material concentration-dependent effects on hADSCs and Saos-2 cells. For both cells, results suggest that scaffolds with higher G and GO concentrations exhibit lower cell metabolic activity. The scaffolds with relatively high concentrations (G5, G7, GO5, and GO7) showed lower metabolic activity, particularly significant at a later stage on day 14. This could be correlated with ROS accumulation till day 14. As shown in Fig. 3, similar to the trend observed for cell metabolic activity, scaffolds with higher filler concentrations (G5, G7, GO5, and GO7) presented higher ROS levels, corresponding to the lower cell metabolic activity. This strong correlation between the metabolic activity and the ROS release level of both cells indicates that the induced ROS seems to be the reason for the toxicity of G and GO, and this effect is material concentration dependent.

Besides, the cell metabolic activity was also analysed and correlated with the ROS release in a material type-dependent manner. As observed from Fig. 3, both cells present lower cell metabolic activity on GO scaffolds than on G scaffolds and this is more significant in the case of hADSC, particularly at a later stage, indicating that GO presented higher
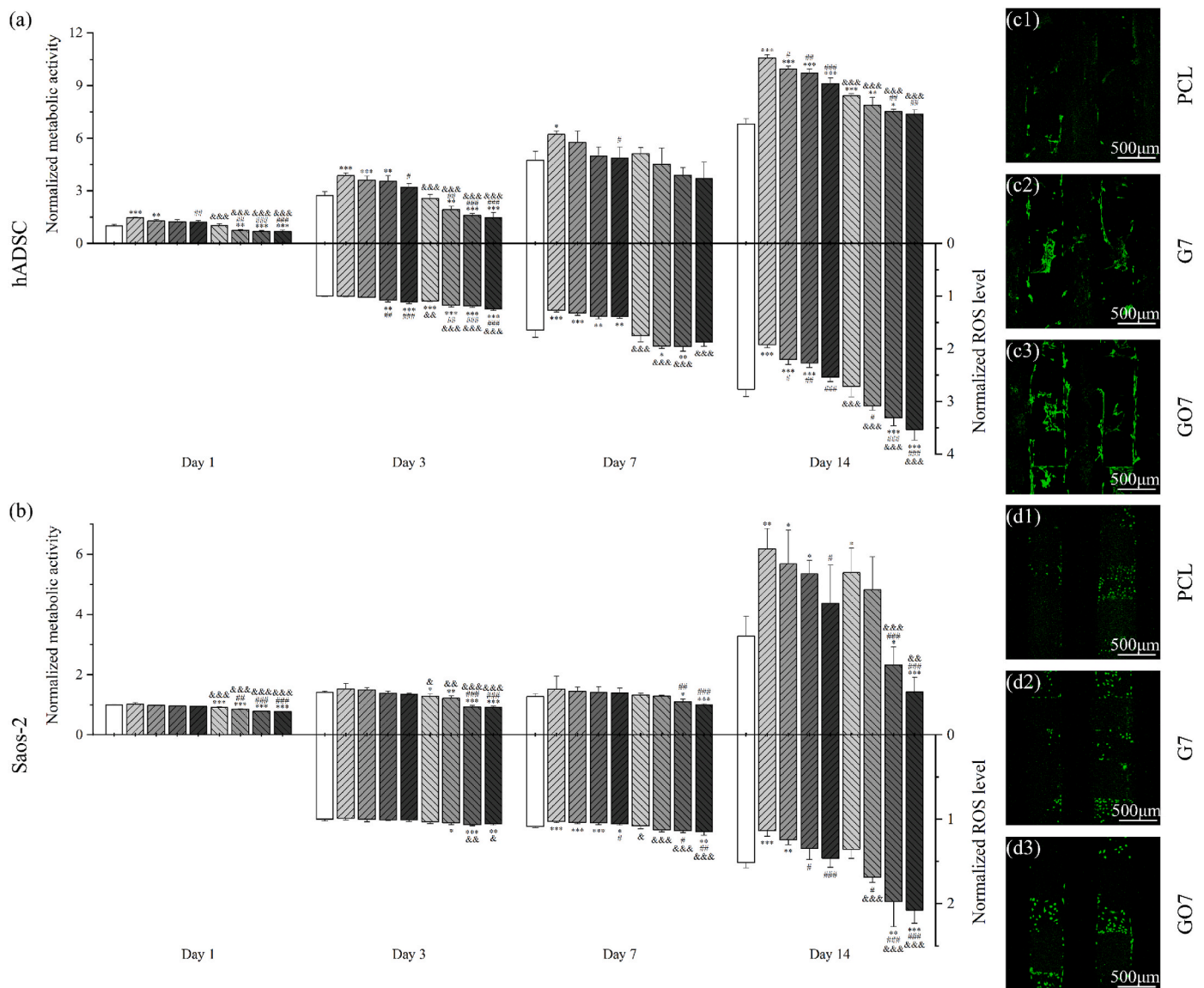
**Fig. 3.** Normalized metabolic activity to PCL scaffolds at day 1 and normalized ROS level to PCL scaffolds at day 1 of hADSCs (a) and Saos-2 cells (b) on PCL, G, and GO scaffolds after 1, 3, 7, and 14 days of cell seeding. Images of hADSC-seeded (c1-3) and Saos-2 seeded (d1-3) PCL, G7, and GO7 scaffolds stained with DCFDA after 7 days of cell seeding. The intensity of the green fluorescence indicates ROS concentration in the cells.

cell toxicity. This can be correlated with the higher ROS release of GO than G due to the richer functional groups (e.g. oxygen, hydroxyl, and carboxyl) of GO.

Moreover, results seem to suggest that Saos-2 is more ROS-sensitive than hADSCs. At day 3, G scaffolds have similar ROS release levels as PCL scaffolds without significant differences. hADSCs on G scaffolds presented statistically higher metabolic activity while this cannot be observed for Saos-2 cells on G scaffolds. This seems to indicate that hADSCs have a larger ROS tolerance. Similar results can be observed on day 14, particularly in the case of GO5 and GO7. Under similar ROS levels that are significantly higher than PCL, GO5 and GO7 scaffolds were still able to sustain hADSCs viability like PCL, while Saos-2 cells on GO5 and GO7 scaffolds presented significantly lower metabolic activity, suggesting that the increased ROS release level has a greater inhibition effect on Saos-2 cells than on hADSCs.

### 3.2. Osteogenic differentiation evaluation and ROS release during differentiation

As shown in Fig. 4, an increasing trend was observed on both ALP activity and calcium deposition (ARS absorbance) comparing day 14 and day 21, suggesting that all scaffolds were able to support hADSC osteogenic differentiation. Cell morphology and calcium deposition on these scaffolds are presented in Fig. 5.

Results showed that the osteogenic differentiation, including both ALP activity and calcium deposition, is dependent on the filler concentrations. As observed, both ALP/total protein concentrations and ARS absorbance are proportional to the filler concentrations. However, statistical differences were not observed at all time points for all scaffolds, and only relatively high concentrations (G5, G7, GO5, and GO7) showed statistically high ALP activity and calcium deposition. Higher ROS level was also observed for scaffolds with higher filler concentration, especially for G7, GO3, GO5, and GO7 scaffolds and this increase is more significant at later differentiation stages (day 21).

However, the effect of graphene-based nanomaterial type on osteogenic differentiation is less significant than graphene-based nanomaterials concentrations. Despite the minor effect of graphene-based nanomaterials type on both ALP activity (only GO7 show a significant difference) and calcium deposition, GO exhibited higher ROS levels during osteogenic differentiation, particularly for GO3, GO5, and GO7 at
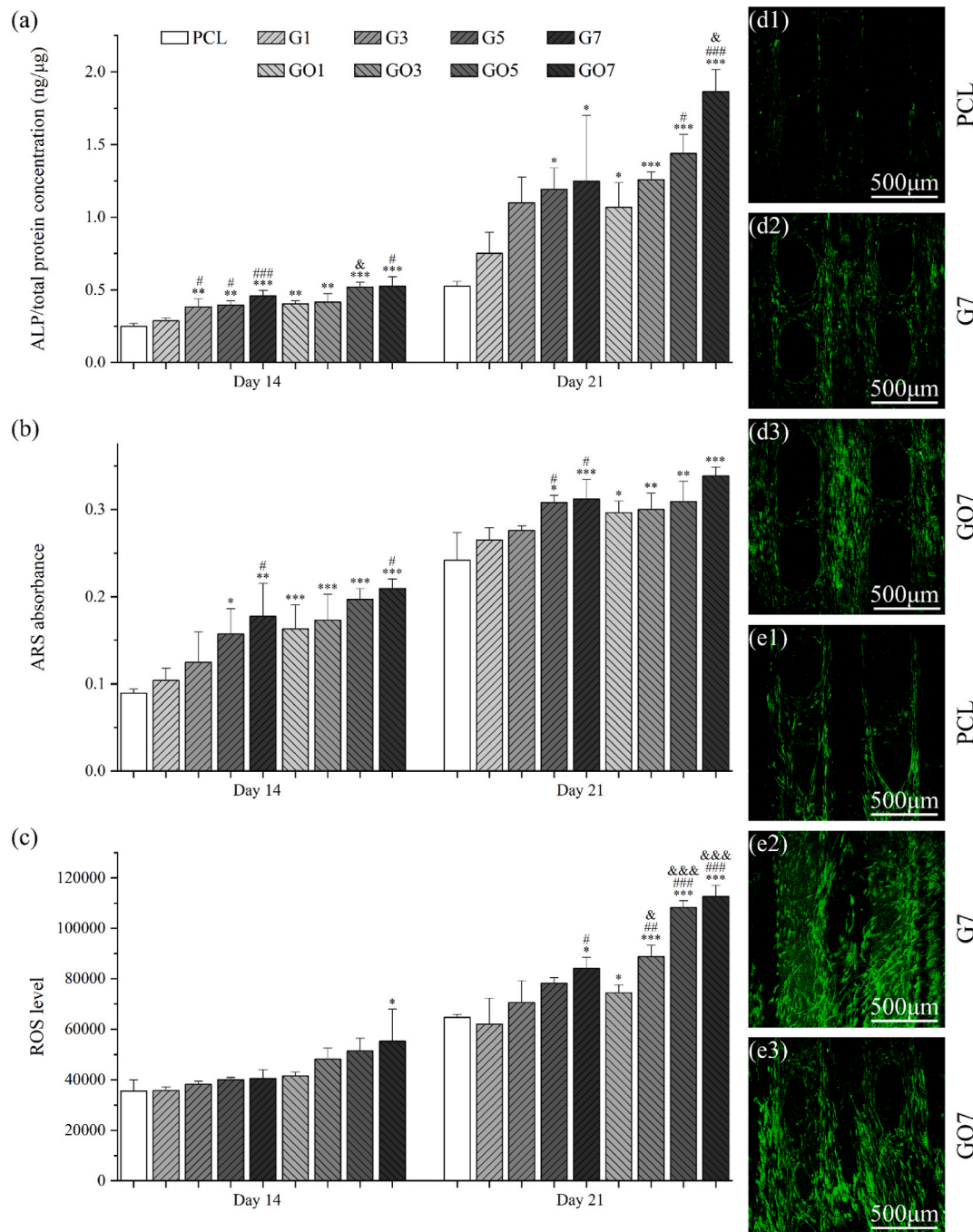
**Fig. 4.** ALP activity (a), calcium deposition (b), and corresponding ROS level (c) of hADSCs on PCL, G, and GO scaffolds at day 14 and day 21 of osteogenic differentiation. Images of hADSC seeded on PCL, G7, and GO7 scaffolds stained with DCFDA at day 14 (d1-3) and day 21 (e1-3) of osteogenic differentiation.

day 21.

## 4. Discussion

The addition of G and GO into PCL scaffolds presents significant impacts on the biological performance of hADSCs and Saos-2 cells, including the metabolic activity during proliferation and osteogenic differentiation. As observed, both G and GO scaffolds exhibited improved hADSCs proliferation and differentiation results than PCL scaffolds, while GO scaffolds with higher concentrations reduced Saos-2 cell proliferation, suggesting a material and concentration dependence. Several mechanisms could explain these effects.

The increased surface hardness of G and GO scaffolds contributes to

improving cell proliferation and differentiation [46–48], as a stiffer surface can stimulate biological responses, influencing cell-surface interactions as well as cell growth, migration, and viability [49–51]. Observed cell proliferation and differentiation results can also be attributed to the increased surface wettability of G and GO scaffolds [52, 53], improving the adsorption of serum proteins that leads to the higher density of adhesion molecules available for cell attachment [48,54], resulting in high cell proliferation and osteogenic differentiation [55, 56]. The increased surface roughness raised by adding G and GO increases the adsorption of proteins and the release of local osteogenic growth factors [57–59], affecting proliferation, and accelerating osteogenesis [48,60,61]. The enhancement, particularly the improved differentiation ability, is more significant in the case of rougher and higher
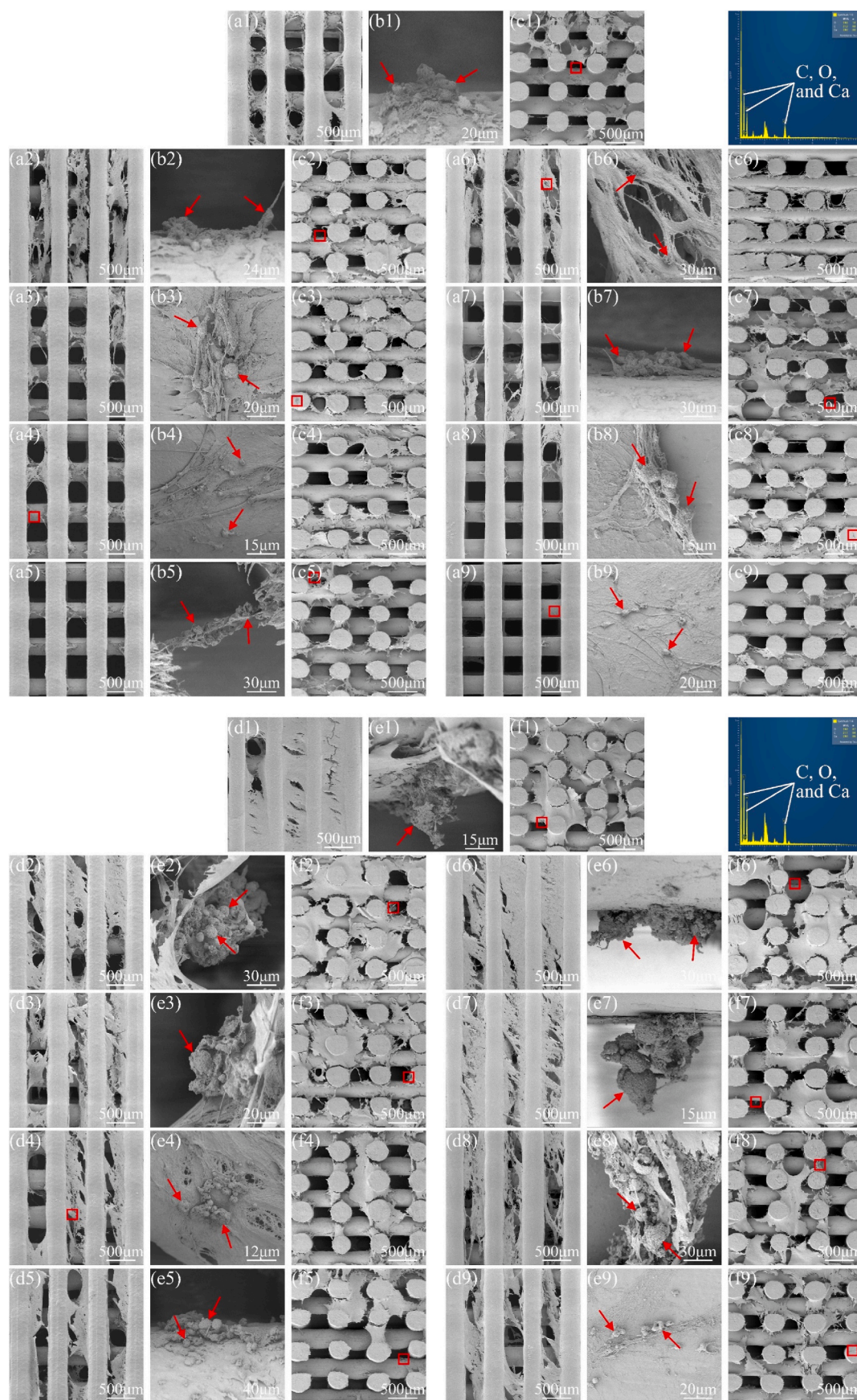
**Fig. 5.** SEM images of hADSCs on PCL, G, and GO scaffolds at day 14 (a) and day 21 (b) of osteogenic differentiation. (1) PCL, (2–5) G1, G3, G5, and G7, (6–9) GO1, GO3, GO5, and GO7. EDX result on the top right and red arrows indicate that there is calcium deposition.
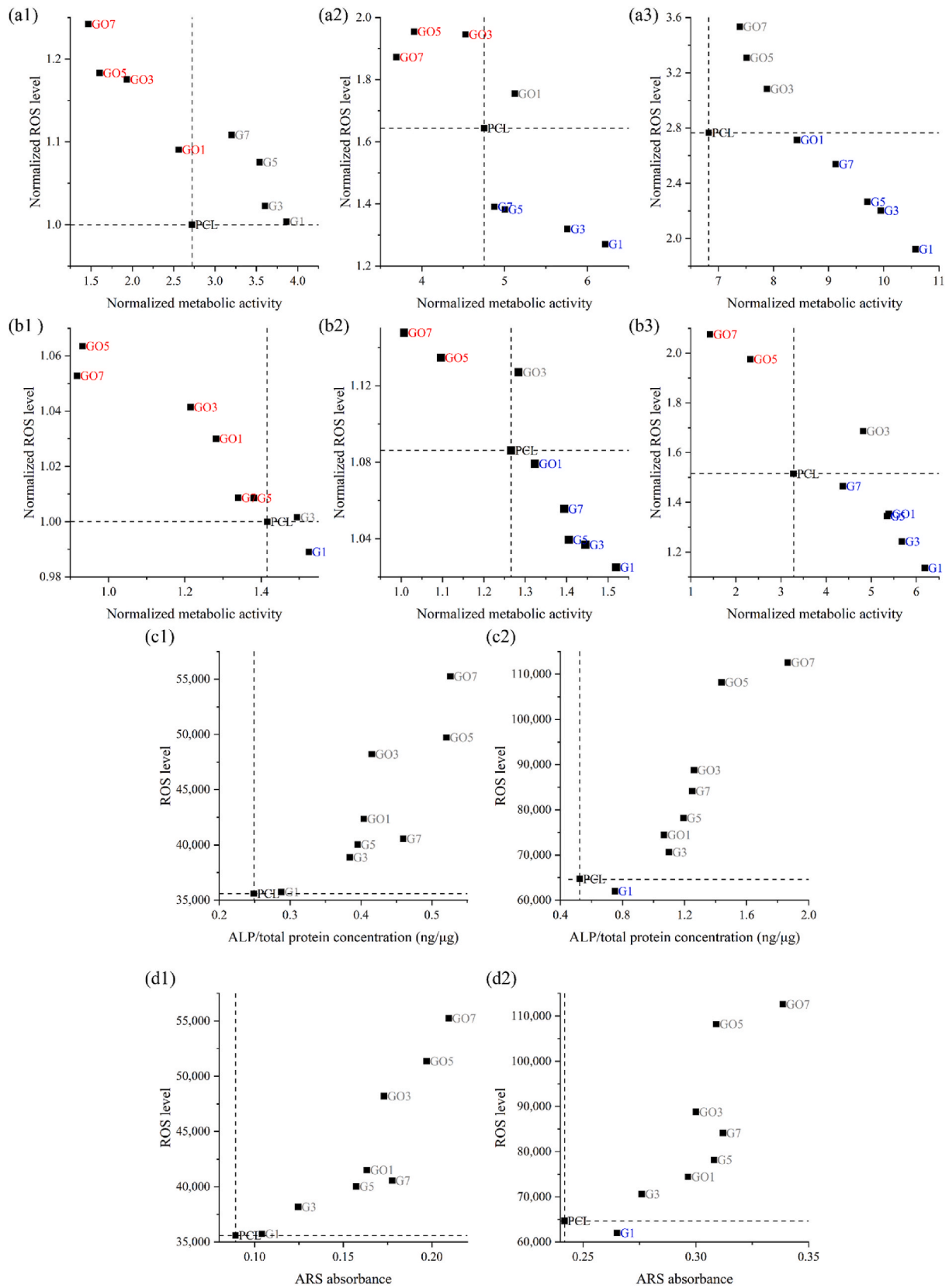
**Fig. 6.** Correlation between normalized cell metabolic activity of hADSCs (a) and Saos-2 cells (b) with normalized ROS level. (1) Day 3, (2) day 7, and (3) day 14. Correlation between ALP activity (c) and calcium deposition (d) of hADSCs with ROS level. (1) Day 14, (2) day 21. Blue groups show increased metabolic activity and differentiation with lower ROS levels, which could be the potential material to have positive effects on cell proliferation and differentiation. Red groups show decreased metabolic activity and differentiation with higher ROS levels, which could be the potential material to have negative effects on cell proliferation and differentiation.

hydrophilic surfaces [61,62]. Besides, the use of these conductive fillers, particularly G, improves the conductivity of the scaffolds, transferring electrical and electromechanical signals to cells [63,64], improving cell-cell signalling and absorption and deposition of serum proteins, thus enhancing cell attachment, proliferation, and osteogenic differentiation *in vitro*, as well as bone formation *in vivo* [65–67]. Preliminary non-biological characterization by the group focusing on the produced scaffolds, including surface characterization (surface roughness, surface hardness and reduced modulus, and surface wettability), *in vitro* degradation characterization, morphological characterization, thermal analysis (thermogravimetric analysis and differential scanning calorimetry analysis), and mechanical characterization, also confirmed these observations [68].

Furthermore, the exposure of cells to G and GO could raise the intracellular ROS level due to the sharp edges of G and GO and charge transfer [69,70], consequently affecting cytotoxicity and genotoxicity [17,70,71]. As shown in this study, GO generates more ROS than graphene-based nanomaterials with lower oxygen content (G), which is aligned with other studies [72,73]. The effect of ROS can be highly relevant to cancer treatment as cancer cells and healthy cells respond differently to ROS. Healthy cells are usually endowed with a low basal level of ROS, while cancer cells have higher ROS levels and reducing equivalents (e.g., NADPH, NADH) due to faster glycolysis (Warburg effect) and pentose phosphate cycle [35,74–76]. Cancer cells also present enhanced antioxidant capacity to avoid ROS-induced cell death [35,75,76], which is a pathophysiological adaptation of cancer cells favouring malignancy [77]. The higher innate ROS levels and concomitant upregulation of antioxidant defence systems of cancer cells lead to lower tolerance of increased ROS levels compared to normal cells [78–80], thus making cancer cells more vulnerable to further ROS production and oxidative stresses [80,81].

To identify the critical concentration of graphene-based nanomaterials for hADSCs and Saos-2 cells and understand the dominant effect of the mechanism mentioned above, different concentrations of G and GO were analysed and catalogued at each time point. For cell proliferation, the positive effects are dominant at lower concentrations (blue groups in Fig. 6a and b, particularly G1) while ROS present more significant effects at higher concentrations (red groups in Fig. 6a and b, particularly GO5 and GO7). It is noteworthy that there is a slight decrease (without significant differences) in Saos-2 cell metabolic activity in PCL groups between day 3 and day 7 (b2 and b1), which may be attributed to the deviation of the experiment (e.g. the presence of air bubbles on the liquid sample surface during the measurement of fluorescence intensity). Regarding cell differentiation (Fig. 6c and d), ROS seems to have a positive impact, but this requires further investigation to decouple the effect of materials and cell differentiation.

## 5. Conclusions

This research investigated 3D-printed PCL scaffolds with different concentrations (1, 3, 5, and 7 wt%) of G and GO and their effect on cell proliferation and differentiation of hADSC and Saos-2 cells. The ROS release level was simultaneously measured to understand how G and GO affect the biological performance of these scaffolds. Results demonstrated that the ROS release from these scaffolds is the dominant mechanism contributing to the inhibition of cell proliferation. Critical concentration thresholds were also identified for both materials as GO5 and GO7 for bone cancer inhibition, and G1 for bone tissue regeneration. Findings also indicate that healthy cells and cancer cells respond differently to the same level of ROS, suggesting that ROS tends to present a stronger inhibition effect on cancer cells. Additionally, cell metabolic activities, ALP activity, and calcium deposition are material- and concentration-dependent. Generally, GO exhibited greater toxicity than G and the cell toxicity increased with material concentrations. The improved hADSCs proliferation (at relatively low concentrations) and differentiation, can be attributed to the improved mechanical and surface properties. While the reduced Saos-2 cell proliferation, which is more significant at relatively high concentrations, can be attributed to the graphene-based nanomaterial induced ROS. These preliminary results reveal the mechanism of how scaffolds containing G and GO affect cell proliferation and osteogenic differentiation. This research also suggests that polymeric scaffolds incorporating graphene-based nanomaterial could be a promising and feasible solution for bone cancer treatment and post-treatment bone regeneration. Future work will focus on further evaluating the effects of materials and cell differentiation using OCN quantification and verifying the mechanism by using immunofluorescence analysis and flow cytometry and then conducting whole-body bioluminescent imaging, haematoxylin-eosin staining, and Masson staining considering rat *in vivo* animal model. Together with this information, it will be possible to optimise the scaffold design, and focus on *in vivo* validation.

## Credit author statement

Conceptualization: Y.H., W.W., and P.B.; Methodology: Y.H., W.W., and P.B.; Investigation: Y.H., W.W., and P.B.; Formal analysis: Y.H., W. W., and P.B.; Validation: Y.H., W.W., and P.B.; Visualization: Y.H., W. W., and P.B.; Writing - original draft: Y.H., W.W., and P.B.; Writing - review & editing: Y.H., W.W., and P.B.; Supervision: W.W. and P.B.; Funding acquisition: W.W. and P.B.

## Declaration of competing interest

The authors declare the following financial interests/personal relationships which may be considered as potential competing interests: Paulo Bartolo reports financial support was provided by Engineering and Physical Sciences Research Council. Weiguang Wang reports financial support was provided by Rosetrees Trust.

## Data availability

Data will be made available on request.

## Appendix A. Supplementary data

Supplementary data to this article can be found online at https://doi.org/10.1016/j.mtbio.2023.100886.

## References

[1] C. Gerrand, N. Athanasou, B. Brennan, R. Grimer, I. Judson, B. Morland, D. Peake, B. Seddon, J. Whelan, G. On behalf of the British Sarcoma, UK guidelines for the management of bone sarcomas, Clin. Sarcoma Res. 6 (1) (2016) 7.
[2] W.F. Enneking, S.S. Spanier, M.M. Malawer, The effect of the anatomic setting on the results of surgical procedures for soft parts sarcoma of the thigh, Cancer 47 (5) (1981) 1005–1022.
[3] G. Bacci, C. Forni, A. Longhi, S. Ferrari, M. Mercuri, F. Bertoni, M. Serra, A. Briccoli, A. Balladelli, P. Picci, Local recurrence and local control of non-metastatic osteosarcoma of the extremities: a 27-year experience in a single institution, J. Surg. Oncol. 96 (2) (2007) 118–123.
[4] Y. Hou, W. Wang, P. Bartolo, Application of additively manufactured 3D scaffolds for bone cancer treatment: a review, Bio-Design Manufact. 5 (3) (2022) 556–579.
[5] Z. Schwartz, A. Somers, J.T. Mellonig, D.L. Carnes Jr., D.D. Dean, D.L. Cochran, B. D. Boyan, Ability of commercial demineralized freeze-dried bone allograft to induce new bone formation is dependent on donor age but not gender, J. Periodontol. 69 (4) (1998) 470–478.
[6] M. Mehta, G.N. Duda, C. Perka, P. Strube, Influence of gender and fixation stability on bone defect healing in middle-aged rats: a pilot study, Clin. Orthop. Relat. Res. 469 (11) (2011) 3102–3110.

[7] R. Eivazzadeh-Keihan, A. Maleki, M. de la Guardia, M.S. Bani, K.K. Chenab, P. Pashazadeh-Panahi, B. Baradaran, A. Mokhtarzadeh, M.R. Hamblin, Carbon based nanomaterials for tissue engineering of bone: building new bone on small black scaffolds: a review, J. Adv. Res. 18 (2019) 185–201.

[8] P. Bellet, M. Gasparotto, S. Pressi, A. Fortunato, G. Scapin, M. Mba, E. Menna, F. Filippini, Graphene-based scaffolds for regenerative medicine, Nanomaterials 11 (2) (2021) 404.

[9] A. Bianco, H.-M. Cheng, T. Enoki, Y. Gogotsi, R.H. Hurt, N. Koratkar, T. Kyotani, M. Monthioux, C.R. Park, J.M.D. Tascon, J. Zhang, All in the graphene family – a recommended nomenclature for two-dimensional carbon materials, Carbon 65 (2013) 1–6.

[10] V.C. Sanchez, A. Jachak, R.H. Hurt, A.B. Kane, Biological interactions of graphene-family nanomaterials: an interdisciplinary review, Chem. Res. Toxicol. 25 (1) (2011) 15–34.

[11] P. Wick, A.E. Louw-Gaume, M. Kucki, H.F. Krug, K. Kostarelos, B. Fadeel, K. A. Dawson, A. Salvati, E. Vázquez, L. Ballerini, M. Tretiach, F. Benfenati, E. Flahaut, L. Gauthier, M. Prato, A. Bianco, Classification framework for graphene-based materials, Angew. Chem. Int. Ed. 53 (30) (2014) 7714–7718.

[12] C. Lee, X. Wei, J.W. Kysar, J. Hone, Measurement of the elastic properties and intrinsic strength of monolayer graphene, Science 321 (5887) (2008) 385.

[13] K.S. Novoselov, A.K. Geim, S.V. Morozov, D. Jiang, Y. Zhang, S.V. Dubonos, I. V. Grigorieva, A.A. Firsov, Electric field effect in atomically thin carbon films, Science 306 (5696) (2004) 666.

[14] N. Krane, Preparation of Graphene, Selected Topics in Physics: Physics of Nanoscale Carbon, 2011, pp. 872–876.

[15] K.V. Emtsev, A. Bostwick, K. Horn, J. Jobst, G.L. Kellogg, L. Ley, J.L. McChesney, T. Ohta, S.A. Reshanov, J. Röhrl, Towards wafer-size graphene layers by atmospheric pressure graphitization of silicon carbide, Nat. Mater. 8 (3) (2009) 203.

[16] S. Guo, S. Dong, Graphene nanosheet: synthesis, molecular engineering, thin film, hybrids, and energy and analytical applications, Chem. Soc. Rev. 40 (5) (2011) 2644–2672.

[17] S. Bengtson, K. Kling, A.M. Madsen, A.W. Noergaard, N.R. Jacobsen, P.A. Clausen, B. Alonso, A. Pesquera, A. Zurutuza, R. Ramos, H. Okuno, J. Dijon, H. Wallin, U. Vogel, No cytotoxicity or genotoxicity of graphene and graphene oxide in murine lung epithelial FE1 cells in vitro, Environ. Mol. Mutagen. 57 (6) (2016) 469–482.

[18] S. Park, R.S. Ruoff, Chemical methods for the production of graphenes, Nat. Nanotechnol. 4 (4) (2009) 217–224.

[19] Q. Mu, G. Su, L. Li, B.O. Gilbertson, L.H. Yu, Q. Zhang, Y.-P. Sun, B. Yan, Size-dependent cell uptake of protein-coated graphene oxide nanosheets, ACS Appl. Mater. Interfaces 4 (4) (2012) 2259–2266.

[20] X.-Q. Wei, L.-Y. Hao, X.-R. Shao, Q. Zhang, X.-Q. Jia, Z.-R. Zhang, Y.-F. Lin, Q. Peng, Insight into the interaction of graphene oxide with serum proteins and the impact of the degree of reduction and concentration, ACS Appl. Mater. Interfaces 7 (24) (2015) 13367–13374.

[21] Y. Wang, Z. Li, J. Wang, J. Li, Y. Lin, Graphene and graphene oxide: biofunctionalization and applications in biotechnology, Trends Biotechnol. 29 (5) (2011) 205–212.

[22] X. Zhang, W. Hu, J. Li, L. Tao, Y. Wei, A comparative study of cellular uptake and cytotoxicity of multi-walled carbon nanotubes, graphene oxide, and nanodiamond, Toxicol. Res. 1 (1) (2012) 62–68.

[23] Y. Li, H. Yuan, A. von dem Bussche, M. Creighton, R.H. Hurt, A.B. Kane, H. Gao, Graphene microsheets enter cells through spontaneous membrane penetration at edge asperities and corner sites, Proc. Natl. Acad. Sci. USA 110 (30) (2013) 12295–12300.

[24] J. Mao, R. Guo, L.-T. Yan, Simulation and analysis of cellular internalization pathways and membrane perturbation for graphene nanosheets, Biomaterials 35 (23) (2014) 6069–6077.

[25] Y. Tu, M. Lv, P. Xiu, T. Huynh, M. Zhang, M. Castelli, Z. Liu, Q. Huang, C. Fan, H. Fang, R. Zhou, Destructive extraction of phospholipids from Escherichia coli membranes by graphene nanosheets, Nat. Nanotechnol. 8 (8) (2013) 594–601.

[26] M. Dallavalle, M. Calvaresi, A. Bottoni, M. Melle-Franco, F. Zerbetto, Graphene can wreak havoc with cell membranes, ACS Appl. Mater. Interfaces 7 (7) (2015) 4406–4414.

[27] O. Akhavan, E. Ghaderi, A. Akhavan, Size-dependent genotoxicity of graphene nanoplatelets in human stem cells, Biomaterials 33 (32) (2012) 8017–8025.

[28] M. Bramini, S. Sacchetti, A. Armirotti, A. Rocchi, E. Vázquez, V. León Castellanos, T. Bandiera, F. Cesca, F. Benfenati, Graphene oxide nanosheets disrupt lipid composition, Ca2+ homeostasis, and synaptic transmission in primary cortical neurons, ACS Nano 10 (7) (2016) 7154–7171.

[29] L. Kovbasyuk, A. Mokhir, Toxicity Studies and Biomedical Applications of Graphene Oxide, Graphene Oxide, 2016, pp. 364–381.

[30] P.P. Fu, Q. Xia, H.-M. Hwang, P.C. Ray, H. Yu, Mechanisms of nanotoxicity: generation of reactive oxygen species, J. Food Drug Anal. 22 (1) (2014) 64–75.

[31] H. Sato, M. Shibata, T. Shimizu, S. Shibata, H. Toriumi, T. Ebine, T. Kuroi, T. Iwashita, M. Funakubo, Y. Kayama, C. Akazawa, K. Wajima, T. Nakagawa, H. Okano, N. Suzuki, Differential cellular localization of antioxidant enzymes in the trigeminal ganglion, Neuroscience 248 (2013) 345–358.

[32] J. Navarro-Yepes, L. Zavala-Flores, A. Anandhan, F. Wang, M. Skotak, N. Chandra, M. Li, A. Pappa, D. Martinez-Fong, L.M. Del Razo, B. Quintanilla-Vega, R. Franco, Antioxidant gene therapy against neuronal cell death, Pharmacol. Therapeut. 142 (2) (2014) 206–230.

[33] M. Deponte, Glutathione catalysis and the reaction mechanisms of glutathione-dependent enzymes, Biochim. Biophys. Acta Gen. Subj. 1830 (5) (2013) 3217–3266.

[34] P. Rajendran, N. Nandakumar, T. Rengarajan, R. Palaniswami, E.N. Gnanadhas, U. Lakshminarasaiah, J. Gopas, I. Nishigaki, Antioxidants and human diseases, Clin. Chim. Acta 436 (2014) 332–347.

[35] A.P. Fernandes, V. Gandin, Selenium compounds as therapeutic agents in cancer, Biochim. Biophys. Acta Gen. Subj. 1850 (8) (2015) 1642–1660.

[36] G. Pizzino, N. Irrera, M. Cucinotta, G. Pallio, F. Mannino, V. Arcoraci, F. Squadrito, D. Altavilla, A. Bitto, Oxidative stress: harms and benefits for human health, Oxid. Med. Cell. Longev. 2017 (2017), 8416763.

[37] Y. Li, Y. Liu, Y. Fu, T. Wei, L. Le Guyader, G. Gao, R.-S. Liu, Y.-Z. Chang, C. Chen, The triggering of apoptosis in macrophages by pristine graphene through the MAPK and TGF-beta signaling pathways, Biomaterials 33 (2) (2012) 402–411.

[38] Y. Wang, J. Wang, H. Hao, M. Cai, S. Wang, J. Ma, Y. Li, C. Mao, S. Zhang, In vitro and in vivo mechanism of bone tumor inhibition by selenium-doped bone mineral nanoparticles, ACS Nano 10 (11) (2016) 9927–9937.

[39] Q. Meng, H. Hu, X. Jing, Y. Sun, L. Zhou, Y. Zhu, B. Yu, H. Cong, Y. Shen, A modular ROS-responsive platform co-delivered by 10-hydroxycamptothecin and dexamethasone for cancer treatment, J. Contr. Release 340 (2021) 102–113.

[40] Y. Hou, W. Wang, P. Bártolo, Novel poly(ε-caprolactone)/graphene scaffolds for bone cancer treatment and bone regeneration, 3D Print. Addit. Manuf. 7 (5) (2020) 222–229.

[41] Y. Hou, W. Wang, P.J.D.S. Bartolo, Investigating the effect of carbon nanomaterials reinforcing poly (ε-Caprolactone) printed scaffolds for bone repair applications, Int. J. Bioprint. 6 (2) (2020) 266.

[42] Y. Hou, W. Wang, P. Bartolo, Investigation of polycaprolactone for bone tissue engineering scaffolds: in vitro degradation and biological studies, Mater. Des. 216 (2022), 110582.

[43] M.H. Hassan, A.M. Omar, E. Daskalakis, Y. Hou, B. Huang, I. Strashnov, B. D. Grieve, P. Bártolo, The potential of polyethylene terephthalate glycol as biomaterial for bone tissue engineering, Polymers 12 (12) (2020) 3045.

[44] E. Daskalakis, B. Huang, C. Vyas, A.A. Acar, F. Liu, A. Fallah, G. Cooper, A. Weightman, G. Blunn, B. Koç, P. Bartolo, Bone bricks: the effect of architecture and material composition on the mechanical and biological performance of bone scaffolds, ACS Omega 7 (9) (2022) 7515–7530.

[45] E. Daskalakis, M.H. Hassan, A.M. Omar, A.A. Acar, A. Fallah, G. Cooper, A. Weightman, G. Blunn, B. Koc, P. Bartolo, Accelerated degradation of poly-ε-caprolactone composite scaffolds for large bone defects, Polymers (2023).

[46] A.J. Engler, S. Sen, H.L. Sweeney, D.E. Discher, Matrix elasticity directs stem cell lineage specification, Cell 126 (4) (2006) 677–689.

[47] J. Blacklock, A. Vetter, A. Lankenau, D. Oupický, H. Möhwald, Tuning the mechanical properties of bioreducible multilayer films for improved cell adhesion and transfection activity, Biomaterials 31 (27) (2010) 7167–7174.

[48] W.C. Lee, C.H.Y. Lim, H. Shi, L.A. Tang, Y. Wang, C.T. Lim, K.P. Loh, Origin of enhanced stem cell growth and differentiation on graphene and graphene oxide, ACS Nano 5 (9) (2011) 7334–7341.

[49] D.E. Discher, P. Janmey, Y.-l. Wang, Tissue cells feel and respond to the stiffness of their substrate, Science 310 (5751) (2005) 1139–1143.

[50] E. Hachet, H. Van Den Berghe, E. Bayma, M.R. Block, R. Auzély-Velty, Design of biomimetic cell-interactive substrates using hyaluronic acid hydrogels with tunable mechanical properties, Biomacromolecules 13 (6) (2012) 1818–1827.

[51] Y. Zeng, J. Yi, Z. Wan, K. Liu, P. Song, A. Chau, F. Wang, Z. Chang, W. Han, W. Zheng, Y.-H. Chen, C. Xiong, W. Liu, Substrate stiffness regulates B-cell activation, proliferation, class switch, and T-cell-independent antibody responses in vivo, Eur. J. Immunol. 45 (6) (2015) 1621–1634.

[52] C. Liang, Y. Luo, G. Yang, D. Xia, L. Liu, X. Zhang, H. Wang, Graphene oxide hybridized nHAC/PLGA scaffolds facilitate the proliferation of MC3T3-E1 cells, Nanoscale Res. Lett. 13 (1) (2018) 15.

[53] A. Lipovka, R. Rodriguez, E. Bolbasov, P. Maryin, S. Tverdokhlebov, E. Sheremet, Time-stable wetting effect of plasma-treated biodegradable scaffolds functionalized with graphene oxide, Surf. Coating. Technol. 388 (2020), 125560.

[54] A. Toffoli, L. Parisi, M.G. Bianchi, S. Lumetti, O. Bussolati, G.M. Macaluso, Thermal treatment to increase titanium wettability induces selective proteins adsorption from blood serum thus affecting osteoblasts adhesion, Mater. Sci. Eng. C 107 (2020), 110250.

[55] Y. Arima, H. Iwata, Effect of wettability and surface functional groups on protein adsorption and cell adhesion using well-defined mixed self-assembled monolayers, Biomaterials 28 (20) (2007) 3074–3082.

[56] A. Ranella, M. Barberoglou, S. Bakogianni, C. Fotakis, E. Stratakis, Tuning cell adhesion by controlling the roughness and wettability of 3D micro/nano silicon structures, Acta Biomater. 6 (7) (2010) 2711–2720.

[57] N. Dubey, R. Bentini, I. Islam, T. Cao, A.H. Castro Neto, V. Rosa, Graphene: a versatile carbon-based material for bone tissue engineering, Stem Cell. Int. 2015 (2015), 804213.

[58] R. Rode, M. Schmid, S. Moghaddam, Protein fouling characteristics of graphene oxide membranes, Adv. Mater. Interfac. 9 (4) (2022), 2101613.

[59] T. Behrouz, S. Behrooz, H. Sarkhosh, M. Nourany, A novel multi-functional model thermoset and PDA-coated PU nanocomposite based on graphene and an amphiphilic block copolymer, Polym. Adv. Technol. 33 (8) (2022) 2480–2497.

[60] L.F. Cooper, Y. Zhou, J. Takebe, J. Guo, A. Abron, A. Holmén, J.E. Ellingsen, Fluoride modification effects on osteoblast behavior and bone formation at TiO2 grit-blasted c.p. titanium endosseous implants, Biomaterials 27 (6) (2006) 926–936.

[61] X. Rausch-fan, Z. Qu, M. Wieland, M. Matejka, A. Schedle, Differentiation and cytokine synthesis of human alveolar osteoblasts compared to osteoblast-like cells (MG63) in response to titanium surfaces, Dent. Mater. 24 (1) (2008) 102–110.

[62] G. Zhao, Z. Schwartz, M. Wieland, F. Rupp, J. Geis-Gerstorfer, D.L. Cochran, B. D. Boyan, High surface energy enhances cell response to titanium substrate microstructure, J. Biomed. Mater. Res. 74 (1) (2005) 49–58.

[63] D.T. Dixon, C.T. Gomillion, Conductive scaffolds for bone tissue engineering: current state and future outlook, J. Funct. Biomater. 13 (1) (2022) 1.

[64] L. Jiang, D. Chen, Z. Wang, Z. Zhang, Y. Xia, H. Xue, Y. Liu, Preparation of an electrically conductive graphene oxide/chitosan scaffold for cardiac tissue engineering, Appl. Biochem. Biotechnol. 188 (4) (2019) 952–964.

[65] J. Li, X. Liu, J.M. Crook, G.G. Wallace, Electrical stimulation-induced osteogenesis of human adipose derived stem cells using a conductive graphene-cellulose scaffold, Mater. Sci. Eng. C 107 (2020), 110312.

[66] N. Zanjanizadeh Ezazi, M.-A. Shahbazi, Y.V. Shatalin, E. Nadal, E. Mäkilä, J. Salonen, M. Kemell, A. Correia, J. Hirvonen, H.A. Santos, Conductive vancomycin-loaded mesoporous silica polypyrrole-based scaffolds for bone regeneration, Int. J. Pharm. 536 (1) (2018) 241–250.

[67] A.G. Guex, J.L. Puetzer, A. Armgarth, E. Littmann, E. Stavrinidou, E.P. Giannelis, G.G. Malliaras, M.M. Stevens, Highly porous scaffolds of PEDOT:PSS for bone tissue engineering, Acta Biomater. 62 (2017) 91–101.

[68] Y. Hou, W. Wang, P. Bartolo, In vitro investigations on the effect of graphene and graphene oxide on polycaprolactone bone tissue engineering scaffolds, Bio-Design Manufact. (2023). In press.

[69] S. Kumar, K. Chatterjee, Comprehensive review on the use of graphene-based substrates for regenerative medicine and biomedical devices, ACS Appl. Mater. Interfaces 8 (40) (2016) 26431–26457.

[70] S. Liu, A. Xu, Y. Gao, Y. Xie, Z. Liu, M. Sun, H. Mao, X. Wang, Graphene oxide exacerbates dextran sodium sulfate-induced colitis via ROS/AMPK/p53 signaling to mediate apoptosis, J. Nanobiotechnol. 19 (1) (2021) 85.

[71] B. Halliwell, M. Whiteman, Measuring reactive species and oxidative damage in vivo and in cell culture: how should you do it and what do the results mean? Br. J. Pharmacol. 142 (2) (2004) 231–255.

[72] I. Francolini, E. Perugini, I. Silvestro, M. Lopreiato, A. Scotto d'Abusco, F. Valentini, E. Placidi, F. Arciprete, A. Martinelli, A. Piozzi, Graphene oxide oxygen content affects physical and biological properties of scaffolds based on chitosan/graphene oxide conjugates, Materials 12 (7) (2019) 1142.

[73] D. Wang, L. Zhu, J.-F. Chen, L. Dai, Can graphene quantum dots cause DNA damage in cells? Nanoscale 7 (21) (2015) 9894–9901.

[74] S. Misra, M. Boylan, A. Selvam, J.E. Spallholz, M. Björnstedt, Redox-active selenium compounds—from toxicity and cell death to cancer treatment, Nutrients 7 (5) (2015) 3536–3556.

[75] S. Arfin, N.K. Jha, S.K. Jha, K.K. Kesari, J. Ruokolainen, S. Roychoudhury, B. Rathi, D. Kumar, Oxidative Stress in Cancer Cell Metabolism, Antioxidants, 2021.

[76] H. Pelicano, D. Carney, P. Huang, ROS stress in cancer cells and therapeutic implications, Drug Resist. Updates 7 (2) (2004) 97–110.

[77] D. Trachootham, J. Alexandre, P. Huang, Targeting cancer cells by ROS-mediated mechanisms: a radical therapeutic approach? Nat. Rev. Drug Discov. 8 (7) (2009) 579–591.

[78] C. Gorrini, I.S. Harris, T.W. Mak, Modulation of oxidative stress as an anticancer strategy, Nat. Rev. Drug Discov. 12 (12) (2013) 931–947.

[79] Q. Kong, J.A. Beel, K.O. Lillehei, A threshold concept for cancer therapy, Med. Hypotheses 55 (1) (2000) 29–35.

[80] E. Panieri, M.M. Santoro, ROS homeostasis and metabolism: a dangerous liason in cancer cells, Cell Death Dis. 7 (6) (2016) e2253-e2253.

[81] T. Li, H. Xu, Selenium-containing nanomaterials for cancer treatment, Cell Rep. Phys. Sci. 1 (7) (2020), 100111.